The Astrophysical Journal, 882:1 (7pp), 2019 September 1 https://doi.org/10.3847/1538-4357/ab3389

CO and Fine-structure Lines Reveal Low Metallicity in a Stellar-mass-rich Galaxy at $z \sim 1$?

C. Lamarche[1], G. J. Stacey[1], A. Vishwas[1], D. Brisbin[2], C. Ferkinhoff[3], T. Nikola[4], S. J. U. Higdon[5], and J. Higdon[5]
[1] Department of Astronomy, Cornell University, Ithaca, NY 14853, USA; cjl272@cornell.edu
[2] Núcleo de Astronomía, Facultad de Ingeniería y Ciencias, Universidad Diego Portales, Av. Ejército 441, 8370191 Santiago, Chile
[3] Department of Physics, Winona State University, Winona, MN 55987, USA
[4] Cornell Center for Astrophysics and Planetary Science, Cornell University, Ithaca, NY 14853, USA
[5] Department of Physics, Georgia Southern University, Statesboro, GA 30460, USA

Received 2019 May 20; revised 2019 July 3; accepted 2019 July 17; published 2019 August 26

Abstract

We present detections of the CO(4–3) and [C I] 609 μm spectral lines, as well as the dust continuum at 480.5 GHz (rest frame), in 3C 368, a Fanaroff–Riley class II (FR-II) galaxy at redshift (z) 1.131. 3C 368 has a large stellar mass, $\sim 3.6 \times 10^{11}\, M_{\odot}$, and is undergoing an episode of vigorous star formation, at a rate of $\sim 350\, M_{\odot}\,\mathrm{yr}^{-1}$, and active galactic nucleus activity, with radio-emitting lobes extended over ~ 73 kpc. Our observations allow us to inventory the molecular-gas reservoirs in 3C 368 by applying three independent methods: (1) using the CO(4–3)-line luminosity, excitation state of the gas, and an α_{CO} conversion factor, (2) scaling from the [C I]-line luminosity, and (3) adopting a gas-to-dust conversion factor. We also present gas-phase metallicity estimates in this source, both using far-infrared fine-structure lines together with radio free–free continuum emission and independently employing the optical [O III] 5007 Å and [O II] 3727 Å lines (R_{23} method). Both methods agree on a subsolar gas-phase metallicity of $\sim 0.3\, Z_{\odot}$. Intriguingly, comparing the molecular-gas mass estimated using this subsolar metallicity, $M_{\mathrm{gas}} \sim 6.4 \times 10^{10}\, M_{\odot}$, to dust-mass estimates from multicomponent spectral energy distribution modeling, $M_{\mathrm{dust}} \sim 1.4 \times 10^{8}\, M_{\odot}$, yields a gas-to-dust ratio within $\sim 15\%$ of the accepted value for a metallicity of $0.3\, Z_{\odot}$. The derived gas mass puts 3C 368 on a par with other galaxies at $z \sim 1$ in terms of specific star formation rate and gas fraction. However, it does not explain how a galaxy can amass such a large stellar population while maintaining such a low gas-phase metallicity. Perhaps 3C 368 has recently undergone a merger, accreting pristine molecular gas from an external source.

Key words: galaxies: evolution – galaxies: high redshift – galaxies: ISM – galaxies: star formation – H II regions – photon-dominated region (PDR)

1. Introduction

Recent studies have made great strides in inventorying molecular gas, the fuel for star formation, in galaxies during the peak epoch of cosmic star formation, redshift (z) ∼1–3, in an effort to determine the efficiency with which these galaxies convert their molecular gas reservoirs into stars (e.g., Tacconi et al. 2010; Harris et al. 2012; Sharon et al. 2016; Harrington et al. 2018; Pavesi et al. 2018). These surveys are complicated by the fact that hydrogen, whose lowest rotational transition takes ∼500 K to excite, is difficult to observe in cold molecular clouds, so that the easily excited low-J rotational levels of carbon monoxide (CO) are generally used as a proxy for molecular gas content. Under some interstellar medium (ISM) conditions, however, appreciable amounts of molecular hydrogen are not accompanied by CO. These so-called "CO-dark" molecular clouds are troublesome in that they cause galaxies containing them to appear very gas poor when employing CO-derived gas-mass estimates. Several possible explanations for these CO-dark molecular clouds exist, including low-metallicity gas present within the ISM of galaxies (e.g., Maloney & Black 1988; Stacey et al. 1991) and highly fractionated molecular clouds (e.g., Stoerzer et al. 1997). Here we investigate one such CO-dark galaxy, 3C 368 (e.g., Evans et al. 1996; Lamarche et al. 2017), which has an appreciable star formation rate (SFR) and seemingly very little molecular gas.

3C 368 was discovered as part of the Third Cambridge Radio Catalog (Edge et al. 1959) and has come to be known as one of the archetypal Fanaroff–Riley class II (FR-II) galaxies. It is an interesting source, situated within the peak epoch of cosmic star formation, forming stars at a rate of $\sim 350\, M_{\odot}\,\mathrm{yr}^{-1}$ (Podigachoski et al. 2015), and containing an active galactic nucleus (AGN) that has launched radio-emitting lobes that span ∼73 kpc (Best et al. 1998a).

In Lamarche et al. (2017) we used both mid- and far-infrared (FIR) fine-structure line observations of 3C 368 to infer the age of the young stellar component present within the source, finding an age of ∼6.5 Myr, consistent with that determined using a multicomponent model for the observed UV-FIR spectral energy distribution (SED) (Drouart et al. 2016). We also presented a non-detection of the CO(2–1) line, constraining the CO luminosity to a level 12 times lower than expected in star-forming galaxies, based on standard ratios with the [C II] 158 μm line (e.g., Stacey et al. 1991), which we attributed to either a low-metallicity or highly fractionated ISM. In this follow-up paper, we present observations of the CO(4–3) and [C I](1–0) 609 μm spectral lines, which emanate from molecular clouds and photodissociation regions (PDRs), respectively, as well as the dust continuum emission at 480.5 GHz (rest frame), in 3C 368, and show how these measurements help us to disentangle these two competing scenarios.

We assume a flat Λ cold dark matter cosmology, with $\Omega_M = 0.27$, $\Omega_\Lambda = 0.73$, and $H_0 = 71\ \mathrm{km\,s^{-1}\,Mpc^{-1}}$, throughout this paper (Spergel et al. 2003).

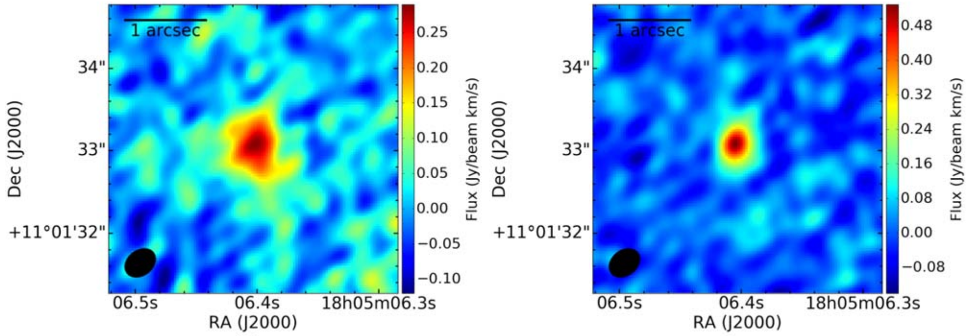

(a) (b)

Figure 1. (a) ALMA CO(4–3) moment-zero map showing the core component of 3C 368 at 0.″4 resolution. The CO-emitting source has a size of 0.″77 × 0.″46, deconvolved from the beam. (b) ALMA [C I] 609 μm moment-zero map showing the same region of 3C 368 at 0.″4 resolution. The deconvolved [C I]-emitting source size is 0.″43 × 0.″23.

Table 1
Spectral Line and Continuum Observations of 3C 368

Observation	Core	Northern Lobe	Southern Lobe	Unit
CO(4–3)	7.8 ± 1.0	⋯	⋯	$F_{\rm obs}$ (10^{-21} W m^{-2})
″	4.6 ± 0.6	⋯	⋯	L' (10^9 K km s^{-1} pc^2)
[C I](1–0)	6.6 ± 0.7	⋯	⋯	$F_{\rm obs}$ (10^{-21} W m^{-2})
″	3.2 ± 0.3	⋯	⋯	L' (10^9 K km s^{-1} pc^2)
Continuum ($\nu_{\rm obs}$ = 225.5 GHz)	96 ± 21	226 ± 59	128 ± 28	$S_{\nu,\rm obs}$ (μJy)

Note. These flux and flux-density values were determined by fitting two-dimensional Gaussian profiles to the respective maps for each of the source components within 3C 368 (see the text).

2. Observations and Data Reduction

2.1. ALMA

The CO(4–3) and [C I] 609 μm lines were observed simultaneously in 3C 368, using the Atacama Large Millimeter/submillimeter Array (ALMA)[6] band-6 receivers. The observations were split into two separate execution blocks: the first conducted on 2016 June 3, with a precipitable water vapor (PWV) measurement of 1.24 mm, and baselines up to 772 m, and the second conducted on 2016 August 20, with a PWV of 0.31 mm, and baselines up to 1462 m. The total on-source integration time for these two observations was ∼1 hr and 40 minutes.

For both execution blocks, J1751+0939 (PKS 1749+096) was used as the bandpass, flux, and phase calibrator. The data from the two execution blocks were reduced using the Common Astronomy Software Application (CASA)[7] ALMA pipeline, version 38366 (C4–R2B), run in CASA version 4.7.0, and subsequently combined, imaged, and cleaned, using CASA version 4.7.2.

Imaging the CO(4–3) measurement set at a spectral resolution of 60 km s^{-1}, and employing a robust parameter of 0.5, we obtain an rms sensitivity of 120 μJy beam^{-1} in each spectral channel, with a synthesized beam of size 0.″41 × 0.″31.

The [C I] 609 μm measurement set was similarly imaged at 60 km s^{-1} spectral resolution, employing a robust parameter value of 0.5. Here we obtain an rms sensitivity of 130 μJy beam^{-1} in each spectral channel, with a synthesized beam of size 0.″39 × 0.″29.

A continuum image was created by combining the two line-free spectral windows present in the measurement set, for a total continuum bandwidth of ∼4 GHz, centered at 225.5 GHz (observed frame). Imaging with a robust parameter value of 0.5, as was done for the line data, we obtain an rms noise of 13 μJy beam^{-1}, with a beam of size 0.″38 × 0.″29.

3. Results and Discussion

3.1. Line and Continuum Fluxes

Both the CO(4–3) and [C I] 609 μm lines are well detected in our ALMA observations, emanating from the core component of 3C 368. A continuum-subtracted moment-zero map was created for each of the two spectral lines (see Figure 1), with the corresponding line fluxes determined by fitting a two-dimensional Gaussian to the emitting region of each moment-zero map. We obtain a CO(4–3) line flux of 1.08 ± 0.14 Jy km s^{-1}, or equivalently $(7.8 \pm 1.0) \times 10^{-21}$ W m^{-2}, and a [C I] 609 μm line flux of 0.85 ± 0.09 Jy km s^{-1}, or equivalently $(6.6 \pm 0.7) \times 10^{-21}$ W m^{-2} (see Table 1). These fluxes were verified by numerically integrating the spectra extracted from an aperture containing the core of 3C 368 (see Figure 2) and were found to be consistent within the quoted uncertainties.

The continuum in 3C 368 is resolved into three components in the 225.5 GHz (observed frame) map: the northern lobe at 226 ± 59 μJy, the southern lobe at 128 ± 28 μJy, and the core at 96 ± 21 μJy (see Figure 3 and Table 1), where these flux densities were determined by fitting a two-dimensional Gaussian to each component in the continuum image. We note that continuum flux extended around the core component of 3C 368 at the same spatial scales as the [C I] and CO emission could be resolved out at the resolution and sensitivity

---

[6] The National Radio Astronomy Observatory is a facility of the National Science Foundation operated under cooperative agreement by Associated Universities, Inc.

[7] https://casa.nrao.edu/

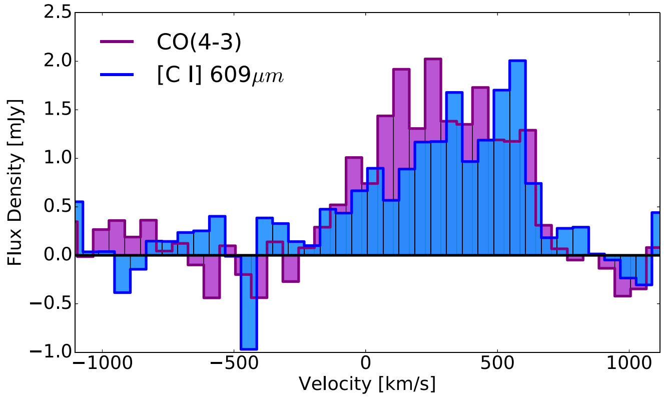

Figure 2. Continuum-subtracted ALMA spectra of both the CO(4–3) and [C I] 609 μm lines extracted from the core component of 3C 368. $v = 0$ corresponds to $z = 1.131$.

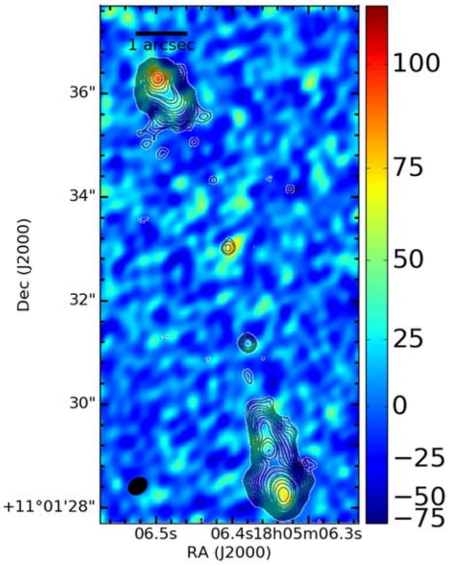

Figure 3. ALMA 225.5 GHz (observed frame) continuum colormap of 3C 368 at 0.″4 resolution. The source is resolved into three components: a core, a northern lobe, and a southern lobe, co-spatial with those seen in 8.21 GHz (observed frame) radio-continuum emission (contour map; Best et al. 1998a). The core component of 3C 368 is unresolved at this resolution and sensitivity.

of our observations, making the quoted flux density from the core a lower limit on the true value.

3.2. Continuum Science

3.2.1. Spectral Energy Distribution

Using the ALMA continuum observations centered at 480.5 GHz (rest frame) presented here, together with our previous ALMA continuum measurements at 205 μm (rest frame; Lamarche et al. 2017), we can calculate the slope of the Rayleigh–Jeans power law for the thermal dust continuum of 3C 368. This is particularly interesting in this case, since the core component of 3C 368, the star-forming galaxy, makes up the smallest contribution to the continuum flux at rest frame 480.5 GHz, the flux being dominated instead by the radio lobes. Hence, unresolved continuum measurements at millimeter/submillimeter wavelengths may have overestimated the flux from the core of 3C 368. We obtain a Rayleigh–Jeans power-law index, $S_\nu \sim \nu^\alpha$, of 3.7 ± 0.4, or equivalently a dust-emissivity β value, $S_\nu \sim \nu^{2+\beta}$, of 1.7 ± 0.4. This is consistent with the dust-emissivity β value assumed in Podigachoski et al. (2015), who used it to derive an FIR luminosity of $2.0 \times 10^{12} L_\odot$, which we used in our previous work and will adopt throughout this paper.

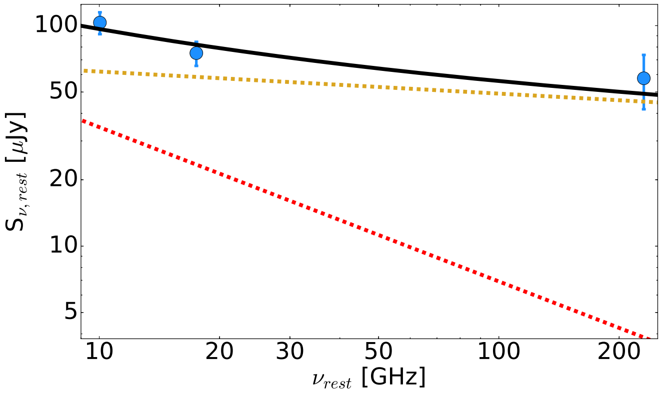

Figure 4. Radio SED of the core component of 3C 368, decomposed into thermal (gold) and nonthermal (red) contributions. Data from Best et al. (1998a) and Lamarche et al. (2017).

We can also decompose the radio SED from the core of 3C 368 into thermal and nonthermal components, using our previous ALMA 230 GHz (rest frame) continuum observations (Lamarche et al. 2017), together with radio-continuum observations at 8.21 and 4.71 GHz (observed frame) (Best et al. 1998a), using an equation of the following form (e.g., Condon 1992; Klein et al. 2018):

$$S_{\mathrm{total},r} = S_{\mathrm{th},0,r}\left(\frac{\nu}{\nu_{0,r}}\right)^{-0.1} + S_{\mathrm{nth},0,r}\left(\frac{\nu}{\nu_{0,r}}\right)^{-\alpha_{\mathrm{nth}}}, \qquad (1)$$

where $S_{\mathrm{th},0,r}$ and $S_{\mathrm{nth},0,r}$ are the (rest frame) contributions to the total radio flux from the thermal and nonthermal components, respectively, at $\nu_{0,r}$ (rest frame), and α_{nth} is the nonthermal power-law index. Adopting a $\nu_{0,r}$ value of 230 GHz and holding α_{nth} fixed at 0.7 (e.g., Shu 1991), we fit for $S_{\mathrm{th},0,r}$ and $S_{\mathrm{nth},0,r}$. We find best-fit values of $S_{\mathrm{th},0,r} = 45 \pm 18$ μJy and $S_{\mathrm{nth},0,r} = 4 \pm 3$ μJy (see Figure 4).

We do not consider any contribution to this part of the SED from thermal dust emission, which continuing the Rayleigh–Jeans power law found above, would contribute only ~5% of the flux measured at 230 GHz (rest frame). Indeed, the continuum flux from the core of 3C 368 is observed to be brighter at rest frame 230 GHz than at rest frame 480.5 GHz, indicating that the dominant emission mechanism at 230 GHz is not thermal dust—an inference made possible by the continuum observations presented here.

Beyond the core component of 3C 368, we note that the radio lobes have considerable emission even in the high-frequency observations presented here (rest frame 480.5 GHz). Between the observed frame 8.21 and 4.71 GHz, Best et al. (1998a) find a spectral index, $S_\nu \sim \nu^\alpha$, of ~−1.5 for both the northern and southern radio lobes. While the flux densities at rest frame 480.5 GHz fall below the extrapolated power-law values, by factors of ~1.4 and 2.3 for the northern and southern lobes, respectively, the fact that such energetic electrons are present within the radio-emitting lobes is noteworthy. While detailed modeling is beyond the scope of this paper, the observations presented here suggest that the radio-emitting lobes of 3C 368 are quite young (e.g., Murgia et al. 1999).

3.2.2. Metallicity From Free–Free Continuum and Far-IR Fine-structure Lines

Having determined that the radio SED of the star-forming core of 3C 368 is dominated by thermal free–free continuum at 230 GHz (rest frame), we can estimate the gas-phase oxygen abundance in 3C 368 using our previous observations of the [O III] 52 μm line (Lamarche et al. 2017).

The method for determining gas-phase absolute ionic abundances using fine-structure line emission and radio free–free continuum has been applied historically to galactic H II regions (e.g., Herter et al. 1981; Rudolph et al. 1997) and more recently to high-redshift galaxies (e.g., Lamarche et al. 2018). This technique provides an alternative to optically derived metallicities, which suffer both from uncertainties in the temperature structure of H II regions, as well as dust extinction of the line flux. Dust obscuration is important in the local universe, especially in the more luminous star-forming galaxies, and becomes an increasingly important effect in the epoch of peak cosmic SFR density, at redshifts ∼1–3. It can be shown that the abundance of ion i, relative to hydrogen, is given by

$$\frac{n_{X^{i+}}}{n_{H^{+}}} = \frac{F_\lambda}{S_{\nu,r}} \frac{4.21 \times 10^{-16} T_4^{-0.35} \nu_9^{-0.1}}{\epsilon_\lambda} \left(\frac{n_e}{n_p}\right), \tag{2}$$

where F_λ is the fine-structure line flux in units of erg s^{-1} cm^{-2}, $S_{\nu,r}$ is the rest-frame radio free–free flux density at rest-frequency ν in units of Jy, T_4 is the electron temperature in units of 10^4 K, ν_9 is the radio emission rest frequency in units of GHz, n_e/n_p is the electron to proton number density ratio, which accounts for the contribution of electrons from non-hydrogen atoms present in the H II regions, and ϵ_λ is the emissivity per unit volume of the fine-structure line at wavelength λ, given by

$$\epsilon_\lambda = \frac{j_{ul}}{n_i n_e} = \frac{h\nu_{ul} A_{ul} n_u}{n_e n_i}, \tag{3}$$

where h is the Planck constant, A_{ul} is the Einstein A coefficient for the line transition at frequency ν_{ul}, 9.8×10^{-5} s^{-1} and 5785.9 GHz, respectively, for the [O III] 52 μm line (Carilli & Walter 2013), and the ratio of the level population in the upper state (n_u) to the total (n_i) is determined by detailed balance. Adopting the collisional coefficients of Palay et al. (2012), and an H II region electron density of 1000 cm^{-3}, as has been determined to be the case in 3C 368 (Lamarche et al. 2017), we calculate a value of $\epsilon_\lambda = 7.6 \times 10^{-22}$ erg s^{-1} cm^3 for the [O III] 52 μm line. We additionally assume $n_e/n_p = 1.05$, which accounts for the electrons contributed from helium, and $T_4 = 1$, a typical value for H II regions.

Combining the total integrated [O III] 52 μm line flux (1.34×10^{-17} W m^{-2}; Lamarche et al. 2017) with the estimated free–free flux density at 230 GHz (rest frame), and using Equation (2), we calculate $[\mathrm{O}^{++}/\mathrm{H}] = 1 \times 10^{-4}$. Then, to determine the $[\mathrm{O}^{++}/\mathrm{O}]$ ratio, and hence scale our ionic oxygen abundance to total oxygen abundance, an estimate for the hardness of the ambient radiation field within 3C 368 is required. Using the H II region models of Rubin (1985), we predicted that ∼84% of the oxygen within the H II regions of 3C 368 is in the O^{++} state (Lamarche et al. 2017). Using that ionization fraction here, we obtain an estimated [O/H] ratio of 1.2×10^{-4}, or $\sim 0.3\, Z_\odot$ (Asplund et al. 2009), within about a factor of 2 uncertainty, where this uncertainty is dominated by both the uncertainty in determining the free–free contribution to the radio SED and the uncertainty in the measured [O III] 52 μm line flux.

This low-metallicity value is consistent with the results of Croxall et al. (2017), who found empirically that the [C II] 158 μm/[N II] 205 μm line ratio is highly elevated in low-metallicity sources. In Lamarche et al. (2017) we found a lower bound of [C II] 158 μm/[N II] 205 μm > 60, which would indicate 12 + log(O/H) ∼8.1, or equivalently $Z \sim 0.25\, Z_\odot$, in the sample from Croxall et al. (2017).

An alternative explanation for the radio emission emanating from the core component of 3C 368 is that it originates from the AGN itself. Strong synchrotron self-absorption can lead to AGN with flat radio spectra, such that the radio emission that we attribute to thermal free–free emission from extended star-forming H II regions may instead come from a compact AGN (e.g., Roellig et al. 1986). As a check on this possibility, we examine the radio/IR correlation, q_{IR} (e.g., Ivison et al. 2010), where

$$q_{\mathrm{IR}} \equiv \log_{10}\left(\frac{S_{\mathrm{IR}}/(3.75 \times 10^{12}\ \mathrm{W\ m^{-2}})}{S_{1.4\,\mathrm{GHz}}/(\mathrm{W\ m^{-2}\ Hz^{-1}})}\right), \tag{4}$$

S_{IR} is the total integrated IR flux (rest frame 8–1000 μm) in units of W m^{-2}, and $S_{1.4\,\mathrm{GHz}}$ is the flux density at 1.4 GHz in units of W m^{-2} Hz^{-1}. Extrapolating the SED-decomposed rest-frame thermal contribution to the radio emission at rest frame 230 GHz (45 μJy) to the expected value at 1.4 GHz using a free–free power-law index of −0.1, and using the total FIR luminosity attributed to star formation in 3C 368 ($2.0 \times 10^{12}\, L_\odot$, Podigachoski et al. 2015) to calculate S_{IR}, we obtain a value of $q_{\mathrm{IR}} = 2.6$. This value is within the range seen in star-forming galaxies (e.g., Ivison et al. 2010), suggesting that the attribution of the radio continuum to free–free emission in 3C 368 is appropriate.

Unfortunately, our 230 GHz rest-frame ALMA observations (Lamarche et al. 2017), with a synthesized beam of size 3″12 × 1″81, do not resolve the core of 3C 368. We will propose higher resolution continuum imaging with ALMA to test the theory of extended H II regions versus compact AGN as the source for the high-frequency radio continuum in 3C 368, thereby supporting or disfavoring the low-metallicity hypothesis for the ISM within 3C 368.

3.2.3. Comparison with Optically Derived Metallicity

The subsolar oxygen abundance that we derive for 3C 368 using the [O III] 52 μm line and radio free–free continuum can be compared to the same value derived using optical lines. Observations exist for 3C 368 in the [O III] 5007 Å, [O II] 3727 Å, and Hδ lines, such that R_{23} (e.g., Pagel et al. 1979) can be calculated by assuming a scaling from Hδ to Hβ, where

$$R_{23} \equiv \frac{[\mathrm{O\,II}]\,\lambda 3727 + [\mathrm{O\,III}]\,\lambda\lambda 4959, 5007}{\mathrm{H}\beta}. \tag{5}$$

Adopting an [O III] 5007 Å line flux of 6.8×10^{-18} W m^{-2} (Jackson & Rawlings 1997), an [O II] 3727 Å line flux of 5.9×10^{-18} W m^{-2} (Best et al. 2000), an Hδ line flux of 2.8×10^{-19} W m^{-2} (Best et al. 2000), and assuming the theoretical scaling of Hδ/Hβ = 0.26 (Case-B recombination,

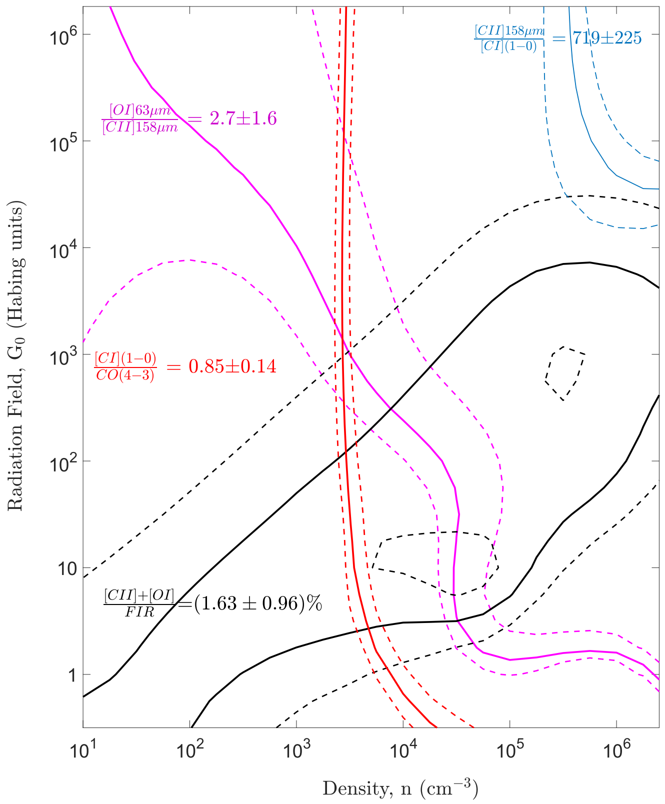

Figure 5. A plot of the best-fit PDR parameters in 3C 368, generated using the models of Pound & Wolfire (2008) and Kaufman et al. (2006). The fit favors PDRs with G_0 ∼320 Habing units and n ∼3200 cm^{-3}.

e.g., Osterbrock & Ferland 2006), we obtain an R_{23} value of ∼12. This R_{23} value indicates 12 + log(O/H) ∼8.3 (Kewley & Dopita 2002), or ∼0.4 $Z_\odot$ (Asplund et al. 2009), making it consistent with the FIR/radio-derived estimate.

3.3. PDRs

3.3.1. PDR Parameters

In Lamarche et al. (2017), we modeled the PDRs within 3C 368, utilizing the PDR Toolbox (Kaufman et al. 2006; Pound & Wolfire 2008), together with detections of the [C II] 158 μm (Stacey et al. 2010) and [O I] 63 μm (Lamarche et al. 2017) lines, as well as the modeled FIR continuum luminosity (Podigachoski et al. 2015), obtaining best-fit parameters of G_0 ∼280 Habing units and n ∼7500 cm^{-3}. Here we update the model to include the two newly detected lines.

Including the CO(4–3) and [C I] 609 μm lines, we obtain new best-fit values of G_0 ∼320 Habing units and n ∼3200 cm^{-3}, with a PDR surface temperature of ∼200 K (see Figure 5). These PDR parameters are similar to those that we obtained previously, up to a decrease in the density, due to the detection significance of the CO(4–3) and [C I] 609 μm lines, which tightly constrain that parameter. We again see that the [C II] emission is high relative to the CO emission, and now also relative to the [C I] emission.

The penetration of far-UV photons capable of photodissociating CO and ionizing carbon is limited by dust extinction. Therefore, assuming dust content scales with metallicity, the CO-photodissociated surface of a molecular cloud becomes much larger relative to the shielded CO-emitting core in low-metallicity environments. In PDR models (e.g., Kaufman et al. 2006), [C I] line emission arises from a thin transition region of neutral carbon that lies between the C^+ and CO regions. The [C II] line flux is therefore enhanced relative to both CO and [C I] in these environments (e.g., Maloney & Black 1988; Stacey et al. 1991).

Table 2
Physical Properties of 3C 368

Property	Value	References
R.A. (J2000)	$18^{h}05^{m}06\overset{s}{.}40$	Best et al. (1998a)
Decl. (J2000)	$+11°01'33\overset{''}{.}09$	Best et al. (1998a)
z	1.131	Meisenheimer & Hippelein (1992)
SFR	350 $M_\odot$ yr^{-1}	Podigachoski et al. (2015)
M_*	3.6×10^{11} $M_\odot$	Best et al. (1998b)
M_{gas}	6.4×10^{10} $M_\odot$	This work
M_{PDR}	1.7×10^{10} $M_\odot$	This work
M_{dust}	1.4×10^{8} $M_\odot$	Podigachoski et al. (2015)
M_{dyn}	$>1.5 \times 10^{11}$ $M_\odot$	This work
δ_{GDR}	464	This work
f_{gas}	0.15	This work
sSFR	1 Gyr^{-1}	This work
SFR/SFR_{MS}	2.8	This work, Genzel et al. (2015)
$\tau_{depletion}$	170 Myr	This work

Note. See the text for explanations of the physical properties presented in this work.

3.3.2. PDR Mass

Using the calculated n, G_0, and PDR surface temperature values in 3C 368, we can estimate the PDR mass following Hailey-Dunsheath et al. (2010):

$$\frac{M_{PDR}}{M_\odot} = 0.77\left(\frac{0.93L_{[C\,II]}}{L_\odot}\right)\left(\frac{1.4\times10^{-4}}{X_{C^+}}\right) \times \frac{1+2\exp\left(\frac{-91\,K}{T}\right)+\frac{n_{crit}}{n}}{2\exp\left(\frac{-91\,K}{T}\right)}, \qquad (6)$$

where X_{C^+} is the abundance of C^+ per hydrogen atom, taken here to be 1.4×10^{-4} (Savage & Sembach 1996), n_{crit} is the critical density of the [C II] 158 μm transition (2800 cm^{-3}, Stacey 2011), and assuming that ∼93% of the [C II] emission originates within the PDRs of 3C 368 as we estimated in Lamarche et al. (2017). We calculate a PDR gas mass of $\sim1.7 \times 10^{10}$ $M_\odot$ in this source (see Table 2).

3.3.3. Molecular Gas Mass

With detections of both the CO(4–3) and [C I] 609 μm lines, the molecular gas mass within 3C 368 can be estimated in three ways:

First, using the detection of the CO(4–3) line, we can estimate the molecular gas mass by assuming a conversion factor back to CO(1–0) and then adopting an α_{CO} value. The measured CO(4–3) line flux of 1.08 ± 0.14 Jy km s^{-1} equates to a value of $L'_{CO(4-3)} = (4.6 \pm 0.6) \times 10^9$ K km s^{-1} pc^2. Our previous non-detection of the CO(2–1) line with ALMA yields a 3σ upper limit of $L'_{CO(2-1)} < 3.45 \times 10^9$ K km s^{-1} pc^2 (Lamarche et al. 2017). This implies that $r_{43/21} > 1.3$, so we use this excitation ratio to scale $L'_{CO(4-3)}$ back to $L'_{CO(1-0)}$. Taking an ultra-luminous infrared galaxy (ULIRG) value of $\alpha_{CO} = 0.8$

$M_\odot (\mathrm{K\,km\,s^{-1}\,pc^2})^{-1}$ (e.g., Bolatto et al. 2013), we obtain a molecular gas mass of $2.9 \times 10^9\,M_\odot$.

If, instead, we calculate a value of α_{CO} based on the metallicity estimates from Section 3.2, adopting the scaling of Glover & Mac Low (2011) (and see also Bolatto et al. 2013), we obtain $\alpha_{\mathrm{CO}} \sim 18\,M_\odot (\mathrm{K\,km\,s^{-1}\,pc^2})^{-1}$. Adopting this larger value of α_{CO}, and assuming the same super-thermal CO excitation as above, we obtain a molecular mass of $6.4 \times 10^{10}\,M_\odot$ (see Table 2). This metallicity-adjusted α_{CO}-based molecular gas mass is $\sim 4\times$ larger than the PDR gas mass estimated above, making the mass ratio consistent with that observed in other starburst galaxies (e.g., Stacey et al. 1991), lending further credibility to the low-metallicity explanation for the small CO luminosity in 3C 368.

The second method is based on a scaling of molecular gas mass with [C I]-line luminosity—which does not assume that the [C I] line arises from a thin transition in the PDRs—as indicated by the work of Papadopoulos et al. (2004). Following Bothwell et al. (2017),

$$M(\mathrm{H_2})^{[\mathrm{C\,I}]} = 1375.8 D_L^2 (1+z)^{-1} \left(\frac{X_{[\mathrm{C\,I}]}}{10^{-5}}\right)^{-1} \times \left(\frac{A_{10}}{10^{-7}\ \mathrm{s^{-1}}}\right)^{-1} Q_{10}^{-1} S_{[\mathrm{C\,I}]} \Delta v, \tag{7}$$

where D_L is the luminosity distance in Mpc (7735 in the case of 3C 368), $X_{[\mathrm{C\,I}]}$ is the $[\mathrm{C\,I}]/\mathrm{H_2}$ abundance ratio, taken here to be 3×10^{-5} (e.g., Weiß et al. 2003; Papadopoulos & Greve 2004), A_{10} is the Einstein A coefficient, $7.93 \times 10^{-8}\ \mathrm{s^{-1}}$ (Wiese et al. 1966), Q_{10} is the excitation parameter, which depends on gas density, kinetic temperature, and radiation field (e.g., Papadopoulos et al. 2004), which we take to be 0.6 (Bothwell et al. 2017), and $S_{[\mathrm{C\,I}]}\Delta v$ is the flux of the [C I] 609 μm line in units of $\mathrm{Jy\,km\,s^{-1}}$. We obtain a molecular gas mass of $2.3 \times 10^{10}\,M_\odot$. We note that this molecular gas mass is $\sim 3\times$ smaller than that derived using the metallicity-corrected α_{CO} method above. If we scale the $[\mathrm{C\,I}]/\mathrm{H_2}$ abundance ratio, $X_{[\mathrm{C\,I}]}$, by the subsolar gas-phase metallicity estimated in Section 3.2, $Z \sim 0.3\,Z_\odot$, we calculate an $\mathrm{H_2}$ mass of $7.7 \times 10^{10}\,M_\odot$. Boosting this mass by ~20% to account for the contribution from helium, which is already accounted for in the α_{CO}-based method above, increases the mass estimate to $9.2 \times 10^{10}\,M_\odot$, such that the two methods produce masses that differ by ~30%.

Finally, we can use the dust mass calculated by multi-component SED modeling, along with a gas-to-dust conversion factor, δ_{GDR}, to estimate the molecular gas mass within 3C 368. Adopting an SED-modeled dust mass of $1.4 \times 10^8\,M_\odot$ (Podigachoski et al. 2015) and a gas-to-dust conversion factor of 540, appropriate for $Z \sim 0.3\,Z_\odot$ (Rémy-Ruyer et al. 2014), we obtain a molecular gas mass of $7.6 \times 10^{10}\,M_\odot$. Or, equivalently, if we use the CO-derived gas mass together with the SED-modeled dust mass, we obtain a value of $\delta_{\mathrm{GDR}} = 464$ (see Table 2). Since α_{CO} and δ_{GDR} scale differently with metallicity, the CO- and dust-derived gas masses are incompatible at solar metallicity, giving us more confidence that 3C 368 does indeed have subsolar metallicity, and that our derived gas masses are robust.

The calculated molecular gas mass implies that, at its current SFR, $\sim 350\,M_\odot\,\mathrm{yr^{-1}}$ (Podigachoski et al. 2015), 3C 368 will deplete its supply of molecular gas in ~170 Myr. We can additionally calculate the gas fraction, $f_{\mathrm{gas}} \equiv \frac{M_{\mathrm{gas}}}{M_{\mathrm{gas}} + M_{\mathrm{stars}}}$, and the specific SFR, $\mathrm{sSFR} \equiv \frac{\mathrm{SFR}}{M_{\mathrm{stars}}}$, in 3C 368, finding values of ~0.15 and $\sim 1\,\mathrm{Gyr^{-1}}$, respectively (see Table 2). The calculated sSFR puts 3C 368 on the upper end of the galaxy main sequence as defined by Genzel et al. (2015), $\mathrm{SFR}/\mathrm{SFR_{MS}} = 2.8$, and the gas fraction lies exactly on the scaling with $\mathrm{sSFR}/\mathrm{sSFR_{MS}}$, stellar mass, and redshift found in Scoville et al. (2017). Moreover, 3C 368 lies along the $L'_{[\mathrm{C\,I}]}$ to L_{IR} correlation found in other high-redshift main-sequence galaxies, however it is elevated in its $L'_{[\mathrm{C\,I}]}/L'_{\mathrm{CO(2-1)}}$ ratio, with a lower limit of 0.9, by a factor of ~4.4 (Valentino et al. 2018). The models of Papadopoulos et al. (2018) find the [C I](1–0)/CO(1–0) brightness ratio to be much larger than unity in low-metallicity or cosmic-ray-dominated regions, however, since we have only a modest lower limit on this ratio, we cannot draw any strong conclusions from it. When compared to a sample of low-metallicity high-redshift sources (Coogan et al. 2019), 3C 368 is observed to be similarly deficient in CO emission, and when compared to a sample of local luminous infrared galaxies and spirals (Liu et al. 2015), it has a CO(4–3) flux that falls below that expected from the scaling with FIR luminosity, by a factor of ~3.7.

3.4. Dynamical Mass

Since our ALMA observations of 3C 368 spatially resolve the source, we can additionally estimate the dynamical mass of the galaxy. Assuming a disk geometry and circular orbits,

$$M_{\mathrm{dyn}} = \frac{v_{\mathrm{rot}}^2 r}{G}, \tag{8}$$

where v_{rot} is the true rotational velocity of the disk, estimated from the observed velocity by correcting for the average inclination angle, $\langle v_{\mathrm{rot}} \rangle \sim \frac{\pi}{2} v_{\mathrm{obs}}$ (e.g., Erb et al. 2006), r is the radius of the line-emitting region of the galaxy, and G is the universal gravitational constant.

We estimate the radius from two-dimensional Gaussian fits to the CO(4–3) moment-zero map ($r = 0.5\,\mathrm{FWHM} = 3.14\,\mathrm{kpc}$). Similarly, we take the observed velocity to be half the FWHM of the CO(4–3) line ($v_{\mathrm{obs}} = 284\,\mathrm{km\,s^{-1}}$). We obtain a dynamical mass of $\sim 1.5 \times 10^{11}\,M_\odot$ (see Table 2). This dynamical mass estimate is $\sim 2\times$ smaller than the estimated stellar mass within 3C 368 ($\sim 3.6 \times 10^{11}\,M_\odot$, Best et al. 1998b), a discrepancy that can be due to the effects of inclination angle and mass profile on the calculated dynamical mass.

4. Conclusions

We have presented detections of the CO(4–3) and [C I] 609 μm spectral lines, as well as the rest frame 480.5 GHz dust continuum, in 3C 368, an FR-II-type galaxy at redshift 1.131.

We have estimated the gas-phase metallicity in 3C 368 using two independent methods: (1) combining the observed [O III] 52 μm fine-structure line flux with radio free–free continuum emission and (2) employing the optical [O III] 5007 Å and [O II] 3727 Å lines (R_{23} technique). Both methods arrive at a consistent gas-phase metallicity of $\sim 0.3\,Z_\odot$.

We have calculated the molecular gas mass within 3C 368 in three independent ways: (1) using the CO(4–3) line luminosity, gas excitation, and a metallicity-adjusted α_{CO} conversion factor, (2) scaling from the luminosity of the atomic carbon line, and (3) adopting a conversion factor from dust mass to molecular gas mass. We find a consistent gas-mass estimate of

$\sim 6.4 \times 10^{10} M_\odot$ across these three methods only when adopting a gas-phase metallicity of $\sim 0.3\ Z_\odot$.

Considering this molecular gas mass, and an SFR of $\sim 350\ M_\odot\ \mathrm{yr}^{-1}$ (Podigachoski et al. 2015), we deduce that 3C 368 has a molecular gas depletion time, $\tau_{\mathrm{Depletion}}$, of ~ 170 Myr. We also calculate a gas fraction, f_{gas}, and specific SFR, sSFR, adopting a stellar mass of $\sim 3.6 \times 10^{11}\ M_\odot$ (Best et al. 1998b), of ~ 0.15 and $\sim 1\ \mathrm{Gyr}^{-1}$, respectively. The calculated sSFR puts 3C 368 on the upper end of the galaxy main sequence, as defined by Genzel et al. (2015), and the gas fraction lies exactly on the scaling with sSFR/sSFR$_{\mathrm{MS}}$, stellar mass, and redshift found in Scoville et al. (2017).

Further observations will allow us to determine whether 3C 368 does indeed have low gas-phase metallicity, if indeed free–free continuum emission dominates the radio spectrum at high frequencies, or whether the AGN is strongly contaminating the emission in those bands. In particular, we will propose higher angular-resolution observations at rest frame 230 GHz to determine whether the radio continuum is extended, as should be the case if it originates from star-forming H II regions, or compact, as would be the case if it is of AGN origin.

We thank the anonymous referee for the insightful comments and detailed suggestions that helped to improve this manuscript. C. L. acknowledges support from an NRAO Student Support Award, SOSPA3-011, and from NASA grant NNX17AF37G. D. B. acknowledges support from FONDECYT postdoctorado project 3170974.

This paper makes use of the following ALMA data: ADS/JAO.ALMA#2015.1.00914.S. ALMA is a partnership of ESO (representing its member states), NSF (USA), and NINS (Japan), together with NRC (Canada) and NSC and ASIAA (Taiwan) and KASI (Republic of Korea), in cooperation with the Republic of Chile. The Joint ALMA Observatory is operated by ESO, AUI/NRAO, and NAOJ.

The National Radio Astronomy Observatory is a facility of the National Science Foundation operated under cooperative agreement by Associated Universities, Inc.

ORCID iDs

C. Lamarche https://orcid.org/0000-0003-1874-7498
D. Brisbin https://orcid.org/0000-0002-4795-419X
C. Ferkinhoff https://orcid.org/0000-0001-6266-0213
S. J. U. Higdon https://orcid.org/0000-0002-4021-7453

References

Asplund, M., Grevesse, N., Sauval, A. J., & Scott, P. 2009, ARA&A, 47, 481
Best, P. N., Carilli, C. L., Garrington, S. T., Longair, M. S., & Rottgering, H. J. A. 1998a, MNRAS, 299, 357
Best, P. N., Longair, M. S., & Roettgering, H. J. A. 1998b, MNRAS, 295, 549
Best, P. N., Röttgering, H. J. A., & Longair, M. S. 2000, MNRAS, 311, 1
Bolatto, A. D., Wolfire, M., & Leroy, A. K. 2013, ARA&A, 51, 207
Bothwell, M. S., Aguirre, J. E., Aravena, M., et al. 2017, MNRAS, 466, 2825
Carilli, C. L., & Walter, F. 2013, ARA&A, 51, 105
Condon, J. J. 1992, ARA&A, 30, 575
Coogan, R. T., Sargent, M. T., Daddi, E., et al. 2019, MNRAS, 485, 2092
Croxall, K. V., Smith, J. D., Pellegrini, E., et al. 2017, ApJ, 845, 96
Drouart, G., Rocca-Volmerange, B., De Breuck, C., et al. 2016, A&A, 593, A109
Edge, D. O., Shakeshaft, J. R., McAdam, W. B., Baldwin, J. E., & Archer, S. 1959, MmRAS, 68, 37
Erb, D. K., Steidel, C. C., Shapley, A. E., et al. 2006, ApJ, 646, 107
Evans, A. S., Sanders, D. B., Mazzarella, J. M., et al. 1996, ApJ, 457, 658
Genzel, R., Tacconi, L. J., Lutz, D., et al. 2015, ApJ, 800, 20
Glover, S. C. O., & Mac Low, M. M. 2011, MNRAS, 412, 337
Hailey-Dunsheath, S., Nikola, T., Stacey, G. J., et al. 2010, ApJL, 714, L162
Harrington, K. C., Yun, M. S., Magnelli, B., et al. 2018, MNRAS, 474, 3866
Harris, A. I., Baker, A. J., Frayer, D. T., et al. 2012, ApJ, 752, 152
Herter, T., Helfer, H. L., Pipher, H. L., et al. 1981, ApJ, 250, 186
Ivison, R. J., Magnelli, B., Ibar, E., et al. 2010, A&A, 518, L31
Jackson, N., & Rawlings, S. 1997, MNRAS, 286, 241
Kaufman, M. J., Wolfire, M. G., & Hollenbach, D. J. 2006, ApJ, 644, 283
Kewley, L. J., & Dopita, M. A. 2002, ApJS, 142, 35
Klein, U., Lisenfeld, U., & Verley, S. 2018, A&A, 611, A55
Lamarche, C., Stacey, G., Brisbin, D., et al. 2017, ApJ, 836, 123
Lamarche, C., Verma, A., Vishwas, A., et al. 2018, ApJ, 867, 140
Liu, D., Gao, Y., Isaak, K., et al. 2015, ApJL, 810, L14
Maloney, P., & Black, J. H. 1988, ApJ, 325, 389
Meisenheimer, K., & Hippelein, H. 1992, A&A, 264, 455
Murgia, M., Fanti, C., Fanti, R., et al. 1999, A&A, 345, 769
Osterbrock, D. E., & Ferland, G. J. 2006, Astrophysics of Gaseous Nebulae and Active Galactic Nuclei (Sausalito, CA: Univ. Science Books)
Pagel, B. E. J., Edmunds, M. G., Blackwell, D. E., Chun, M. S., & Smith, G. 1979, MNRAS, 189, 95
Palay, E., Nahar, S. N., Pradhan, A. K., & Eissner, W. 2012, MNRAS, 423, L35
Papadopoulos, P. P., Bisbas, T. G., & Zhang, Z.-Y. 2018, MNRAS, 478, 1716
Papadopoulos, P. P., & Greve, T. R. 2004, ApJL, 615, L29
Papadopoulos, P. P., Thi, W. F., & Viti, S. 2004, MNRAS, 351, 147
Pavesi, R., Sharon, C. E., Riechers, D. A., et al. 2018, ApJ, 864, 49
Podigachoski, P., Barthel, P. D., Haas, M., et al. 2015, A&A, 575, A80
Pound, M. W., & Wolfire, M. G. 2008, in ASP Conf. Ser. 394, Astronomical Data Analysis Software and Systems XVII, ed. R. W. Argyle, P. S. Bunclark, & J. R. Lewis (San Francisco, CA: ASP), 654
Rémy-Ruyer, A., Madden, S. C., Galliano, F., et al. 2014, A&A, 563, A31
Roellig, T. L., Becklin, E. E., Impey, C. D., & Werner, M. W. 1986, ApJ, 304, 646
Rubin, R. H. 1985, ApJS, 57, 349
Rudolph, A. L., Simpson, J. P., Haas, M. R., Erickson, E. F., & Fich, M. 1997, ApJ, 489, 94
Savage, B. D., & Sembach, K. R. 1996, ARA&A, 34, 279
Scoville, N., Lee, N., Vanden Bout, P., et al. 2017, ApJ, 837, 150
Sharon, C. E., Riechers, D. A., Hodge, J., et al. 2016, ApJ, 827, 18
Shu, F. H. 1991, The Physics of Astrophysics (Mill Valley, CA: Univ. Science Books)
Spergel, D. N., Verde, L., Peiris, H. V., et al. 2003, ApJS, 148, 175
Stacey, G. J. 2011, ITTST, 1, 241
Stacey, G. J., Geis, N., Genzel, R., et al. 1991, ApJ, 373, 423
Stacey, G. J., Hailey-Dunsheath, S., Ferkinhoff, C., et al. 2010, ApJ, 724, 957
Stoerzer, H., Stutzki, J., & Sternberg, A. 1997, A&A, 323, L13
Tacconi, L. J., Genzel, R., Neri, R., et al. 2010, Natur, 463, 781
Valentino, F., Magdis, G. E., Daddi, E., et al. 2018, ApJ, 869, 27
Weiß, A., Henkel, C., Downes, D., & Walter, F. 2003, A&A, 409, L41
Wiese, W. L., Smith, M. W., & Glennon, B. M. 1966, Atomic Transition Probabilities. Vol. Hydrogen through Neon. A Critical Data Compilation (Washington, DC: National Bureau of Standards)